

Using Polar Faculae to Determine the Sun’s High-Latitude Rotation Rate. II: Simulations and New Measurements

NEIL R. SHEELEY, JR.¹

¹*Visiting Research Scientist
Lunar and Planetary Laboratory, University of Arizona
Tucson, AZ 85721, USA*

ABSTRACT

In a previous paper, I described a new way of determining the high-latitude solar rotation rate statistically from space-time maps of polar faculae observed in the 6767 Å continuum by the Michelson Doppler Interferometer (MDI) on the *Solar and Heliospheric Observatory* (SOHO) (Sheeley 2024). Now, I have tested the technique by applying it to simulated images whose faculae have known speeds, and I have been able to recover those speeds with an accuracy better than 0.01 km s⁻¹. Repeated measurements of the Sun’s polar faculae gave the same high-latitude profile as before, but with a slightly faster synodic rotation rate of 9.°10 day⁻¹ and a rotation period of 39.6 days. Applying this space-time tracking procedure to magnetic flux elements observed with the Helioseismic Magnetic Imager (HMI) on the *Solar Dynamics Observatory* (SDO), I obtained a similar rotation profile with a speed of 9.°55 day⁻¹ and a synodic rotation period of 37.7 days. These rates are comparable to polar rotation rates, obtained by other techniques, but the new latitude profiles are noticeably flatter than the quartic fits to those prior measurements.

Keywords: Solar faculae (1494)— Solar rotation (1524)—Solar magnetic fields (1503)—Solar cycle (1487)

1. INTRODUCTION

This is the second of two papers about measuring the Sun’s rotation rate at high latitudes by tracking polar faculae. In paper I, I made space-time maps from latitude slices of 6767 Å continuum images obtained during 7-21 February, 1997-1998 with the Michelson Doppler Interferometer (MDI) on the *Solar and Heliospheric Observatory* (SOHO). Each space-time map showed a collection of parallel tracks whose average slope indicated the longitudinal speed of the faculae at that latitude. By plotting those speeds versus latitude, I found that the points fell along a straight line whose slope was about 1.90 km s⁻¹, and whose extension went through 0 km s⁻¹ at the Sun’s south pole with an rms scatter $\lesssim 0.03$ km s⁻¹. This gave a nearly constant angular speed of approximately 8.°6 day⁻¹ over a cap within about 30° of the pole.

Comparison with past measurements of the angular rotation rate of polar faculae by Müller (1954) and Waldmeier (1955) gave values closer to 9.°00 day⁻¹, suggesting that my new values may have been slightly too slow. Consequently, I generated a series of images containing simulated faculae, whose speeds were assigned the rotation profile

$$\frac{v_\phi}{v_0} = \frac{90 - \lambda}{90}, \quad (1)$$

where v_ϕ is the azimuthal component of solar rotation at the latitude, λ (in degrees), and $v_0 = 2$ km s⁻¹. By applying this space-time approach to the simulated data, I was able to recover the speed of the simulated faculae within 0.01 km s⁻¹.

This paper is organized as follows. Section 2 concerns the simulations, including their images, their space-time maps, and their measurements. Section 3 returns to the solar observations, including the MDI 6767 Å faculae, the HMI magnetic flux elements, and a comparison of their space-time measurements with prior measurements using other techniques. Section 4 provides a summary and discussion of the results. Appendices A and B provide analytical calculations of the B_0 angle and what to expect from space-time measurements using a straight slit and a slit that is

curved along the latitude contours. Finally, Appendix C contains a discussion of the way that pixelation of the image affects alternate methods of calibrating the chord length.

2. THE SIMULATIONS

2.1. Simulated Images

The idea of generating a series of simulated solar images containing polar faculae seemed daunting at first. But then I realized that I could do it fairly quickly with the help of ChatGPT, which would provide most of the essential code. Consequently, I asked ChatGPT to write a program that would scatter a number of bright points at random within a 60-90° region around the simulated north pole, and then start them rotating with the profile given by Eq(1). I did not space them uniformly in area, as one might expect for solar faculae whose fields would be concentrated at regularly spaced supergranular boundaries. Also, I did not give them finite lifetimes and insert new faculae to replace older faculae that have died, as one would expect for real faculae that were subject to a random walk by non-stationary supergranular cells. These simulated faculae were just bright dots moving on latitude contours around the north pole with the specified speed. To aid in my check that ChatGPT had assigned the speeds correctly, I asked that the simulated faculae be color coded with red in the interval 60-65°, yellow in the interval 70-75°, and white elsewhere. (Later, when I made space-time maps, this color-coding provided an unexpected bonus for characterizing the tracks.)

When I was satisfied that ChatGPT had done this task correctly, I asked that the simulated Sun be displayed as seen from a point on the equator in January and June when the Sun's poles were equidistant from Earth. This involved a 90° rotation from the north polar view that Chat used to insert the faculae and get us started. So I calculated the xyz components of faculae whose $r\theta\phi$ components were known. Although ChatGPT may have been able to do that too, I needed the line-of-sight x -component in order to tell ChatGPT how to avoid plotting backside faculae in these frontside images. Finally, to keep the simulated images simple and not confuse ChatGPT, I decided to work in the northern hemisphere. So I asked for the z -axis to be rotated through a B_0 angle of +6.8°, as one would expect in the 7-21 August time-frame, analogous to the -6.8° tilt angle during the 7-21 February interval that was used for the MDI solar images in paper I.

Figure 1 shows a simulated image of the north polar cap as seen from Earth or from the SOHO spacecraft located at the L1 point on the Sun-Earth line, only 1% of the distance to the Sun. Here, the four orange dots at the limb indicate positions that I used to define the slit. In this case, the (row, column) pixel values were (50, 354), (50, 671) at the upper edge of the slit and (55, 340), (55, 685) at the lower edge. These numbers refer to the rows and columns as (row, column), and because the slit was a rectangle, only the numbers 50, 55, 340, 685 at the lower ends of the

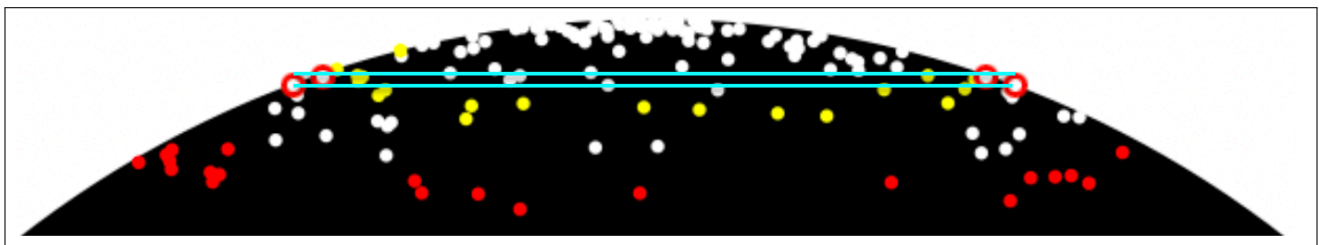


Figure 1. Image of the simulated north polar cap when $B_0 = +6.8^\circ$, corresponding to the south polar cap as it would look during 7-21 February. Faculae were assigned randomly to the 60-90° range. Faculae are white, except those in the 60-65° latitude range, which are red, and those in the 70-75° range, which are yellow. Orange points at the limb define the slit whose north and south boundaries are shown in cyan color, and whose separation was 5 pixels (a sky-plane distance $\sim 7,000$ km).

slit were used. The upper edge of the slit extends a little bit beyond the limb, giving the upper and lower edges of the space-time map a jagged appearance, as will be obvious when we inspect the next two figures. The disk center occurred at row 514, and the solar radius, R_\odot , was 490 pixels in length. Consequently, the ‘y-values’ of the upper and lower edges of the slit were $y_1/R_\odot = (514 - 50)/490 = 0.947$ and $y_2/R_\odot = (514 - 55)/490 = 0.937$. These values are related to the latitude, λ , and the effective tilt angle, $B_0 = 6.8^\circ$, by the equation

$$\frac{y}{R_\odot} = \sin(\lambda - B_0). \quad (2)$$

Here, λ refers to the latitude where the edge of the slit in question crosses the central meridian (since the slit spans a range of heliographic latitudes when $B_0 \neq 0$). Consequently, Eq(2) gives $\lambda_1 = 78.05^\circ$, corresponding to the shorter

edge of the slit, and $\lambda_2 = 76.^{\circ}31$, corresponding to the longer edge. The average and difference of these two latitudes are $\langle \lambda \rangle = 77.^{\circ}18$ and $\Delta\lambda = 1.^{\circ}74$, respectively.

2.2. Space-Time Maps

Next, I used these simulated images to make a space-time map of faculae. From each image, like that in Figure 1, I extracted the narrow rectangular region bounded by the slit, and placed it vertically in chronological order with similar regions at other times to form a rectangular map of ‘slit length’ (along the vertical axis) and time (along the horizontal axis). (I left the original geometry intact, and did not attempt to compress the regions by averaging their original y-dimensions prior to assembling them in the stack.) Therefore, because each slit enclosed a nearly trapezoidal section of the disk, the chronological placement of about 90 such strips caused the resulting space-time map to have serrated upper and lower edges.

Figure 2 shows the space-time map constructed for the slit at $\langle \lambda \rangle = 77.^{\circ}18$ shown in Figure 1. There is a temptation to think of these space-time maps as having the format of Carrington maps with north at the top, south

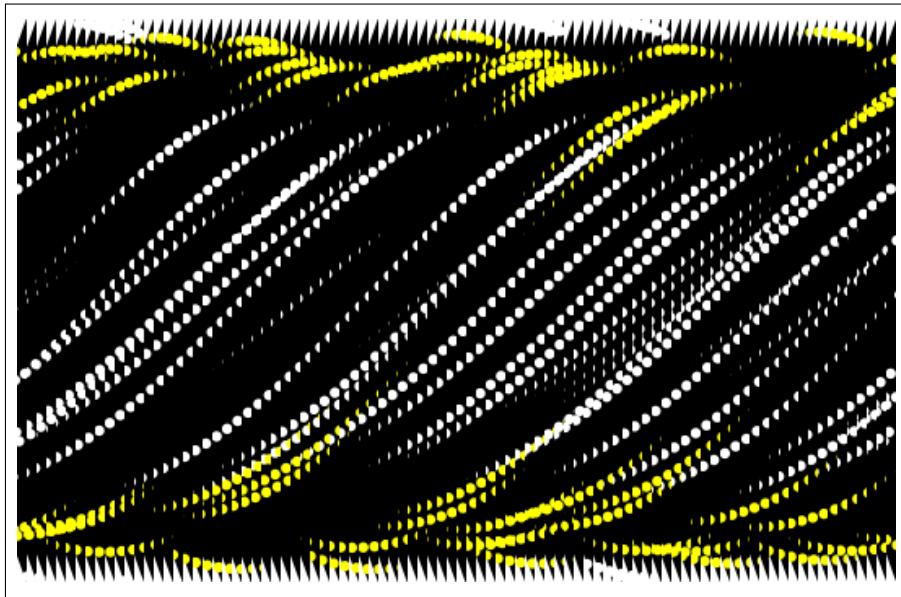


Figure 2. Space-time map obtained from 90 simulated images like that in Figure 1, spanning a 30-day interval with a speed profile given by Eq(1). Located at $\langle \lambda \rangle = 77.^{\circ}18$, the 5-pixel (~ 7 Mm) slit produced the jagged appearance at the upper and lower edges of the map. White sinusoidal tracks at central meridian are from 0.28 km s^{-1} faculae at $\sim 77^{\circ}$. Yellow tracks toward the limbs are from faculae in the $70\text{-}75^{\circ}$ band, and the white tracks at the extreme limbs are from faculae in the $66\text{-}69^{\circ}$ range.

at the bottom, east on the left, and west at the right. However, the format of the space-time maps is just the opposite. The east and west limbs lie at the jagged upper and lower edges, and north and south directions are on the left and right sides. The detailed assignment of directions depends on whether the map was made from the north or the south polar region. For example, the map in Figure 2 was made from narrow, 5-pixel slices of the north polar region. Looking at the jagged edges at the top and bottom of the map, one can see that the individual strips are shorter on their left sides than on their right sides, implying that north is to the left and the south is to the right. This means that west is up and east is down. Consequently, the long, white tracks of positive slope indicate faculae moving from east to west, consistent with time increasing to the right along the bottom of the map. In this paper, I have shown all of the space-time maps this way, with the west limb on top, the east limb on the bottom, and time increasing to the right.

Now, let us return to the details of Figure 2 and their relation to the distribution of simulated faculae in Figure 1. Notice that the long, white, quasi-parallel tracks near the central meridian fade out and are replaced by short, yellow tracks at locations toward the east and west limbs. This transition is due to the non-zero value of B_0 , whose value of $+6.^{\circ}8$ causes the latitude contours in Figure 1 to bend upward toward the limbs. Here, the slit was placed at $77.^{\circ}18$ in a region of white faculae near disk center and well above the $70\text{-}75^{\circ}$ band of yellow faculae. But toward the limbs, the contours of this lower-latitude band of yellow faculae bend upward across the slit., and are visible as short, yellow

tracks in the space-time map. In the jagged regions even closer to the limbs, a few white tracks of negative slope have replaced some of these yellow tracks.

As discussed in Appendix B.0.2, the physical reason for the speed reversal is that the azimuthal positions (i.e. the ϕ angle) of the faculae have reached 90° . At greater distances from central meridian, ϕ is larger than 90° , and the tangential component of speed begins pointing inward along the slit, causing the white tracks of these inward motions to be visible in the serrated regions at the extreme limbs. However, if B_0 were zero, the white tracks at the central meridian would retain their idealistic sinusoidal shapes, and extend all the way to the limb without these complications. Regardless of this interesting behavior toward the ends of the slit, the main point of Figure 2 is that nearly linear, parallel tracks are visible around the center of the slit, and if one confines the measurements to that region, one can determine the tangential velocity of the simulated faculae at this latitude relatively easily.

Recall that the simulated faculae were created with infinite lifetimes, rather than the 1-2-day lifetimes of polar faculae on the Sun. Consequently, the tracks of simulated faculae are continuous, whereas the tracks of most polar faculae consist of shorter 1-2-day segments during the 2-3 week time that it would take for them to transit the solar disk at their observed speeds. Nevertheless, because the shorter tracks of real faculae are essentially parallel, it is still easy to fit their average slope with a straight line. In retrospect, I suspect that, with ChatGPT's help, it would have been easy to create simulated faculae with finite lifetimes, and maintain an equilibrium by creating new faculae continuously as old faculae die. In this new era of artificial intelligence (AI), I suspect that difficult problems, that we once might have avoided, can be done easily, and that our results are only limited by our imaginations.

Figure 3 shows another space-time map obtained at an average latitude $\langle \lambda \rangle = 68.^\circ 52$ with a 5-pixel slit. In this case, $\Delta\lambda = 1.^\circ 23$ and $v = 0.49 \text{ km s}^{-1}$. This time the slit was positioned in the cloud of white faculae in the $66\text{-}69^\circ$ region just poleward of the $60\text{-}65^\circ$ band of red faculae. Consequently, the quasi-linear tracks near the center of the slit

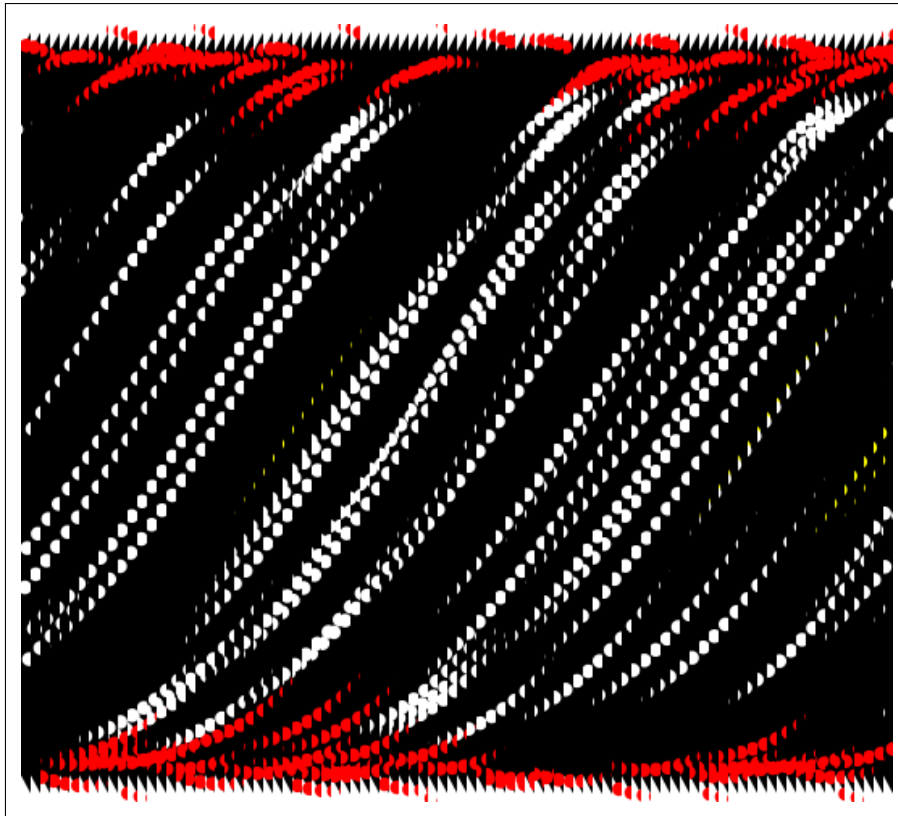


Figure 3. Same as Figure 2, except that the 5-pixel slit was placed at $\langle \lambda \rangle = 68.^\circ 52$ in the region of white faculae just poleward of the $60\text{-}65^\circ$ band of lower-latitude red faculae. Again, a series of quasi-parallel white tracks dominates the center of the slit, giving a speed of 0.49 km s^{-1} , while curved and reversed speed red tracks are visible toward the ends of the slit.

are white and the curved tracks toward the ends of the slit are red. In fact, one can even see red tracks of negative slope in the jagged regions at the extreme ends of the slits.

Because the slit used in Figure 3 was placed at a lower latitude than the slit used in Figure 2 ($68.^\circ52$ compared to $77.^\circ18$), the white faculae remain on the slit for a greater fraction of the slit length than they did in Figure 2. Consequently, in Figure 3 the sinusoids are relatively longer and the remaining short tracks are confined closer to the limbs than they were in Figure 2. This dependence on latitude is discussed toward the end of Appendix B.0.2.

2.3. Speed Measurements

Figures 2 and 3 are printed to scale in the sense that they have equal horizontal dimensions of 30 days and vertical dimensions equal to the distance between the black peaks in the serrated edges at the top and bottom of the space-time maps. This vertical distance is the length, Δx_2 , of the chord at the longer edge of the slit. In paper I, I determined this chord length (in pixels) by subtracting the measured x_2 -values at the opposite ends of the slit. This was very easy to do because the intensity fell off rapidly at the limb, and I defined the end point by the last bright pixel in that row.

When I began to track the simulated faculae in this paper, I decided to evaluate the chord length (in units of solar radii) in terms of λ_2 , the latitude of the longer edge of the slit. I had already determined λ_2 using the relation $y/R_\odot = \sin(\lambda_2 - B_0)$, and I thought that there was no need to introduce possible errors associated with the independent measurement of the x coordinates. This alternate approach introduces pixelation errors on the order of a pixel size divided by the length of a chord, and so probably does not affect the simulation images whose radii are 490 pixels. But, as we shall see later, the solar images have radii of 246 pixels (for MDI faculae) and 235 pixels (for HMI magnetic elements), so for those solar images, I returned to the original approach of determining the chord length by subtracting the observed coordinates at the ends of the slit. It turned out that the resulting speed measurements were almost unaffected, so that either procedure would have been satisfactory. This pixelation effect is described in more detail in Appendix C.

Initially, I wondered how well I could align a ruler so that it was parallel to the tracks of faculae in the space-time map. When tracks were plentiful, I tried to align the ruler so that both of its parallel edges followed along the tracks of different faculae, thinking that would increase the reliability (which perhaps it did). Still, I wondered how accurate the result would be. I found that after measuring slopes over a range of latitudes, the points fell along a straight line, and that the polar intercept of that line was nearly 0 km s^{-1} , with accuracies in the range $0.01\text{-}0.03 \text{ km s}^{-1}$. This was particularly surprising because I had made the measurements in no particular order of latitude, so without my knowledge, the procedure had reordered the measurements so that they fell almost precisely along a straight line aimed toward 0 km s^{-1} at the pole. The results were even more accurate for the simulated faculae (with an rms deviation of the data points from the line by less than 0.01 km s^{-1}). Nevertheless, there were some reproducible outliers in the solar measurements (see Figure 9 below), indicating that an occasional space-time map was able to fool me into making an inaccurate measurement.

So, I evaluated the tangential speed, v_ϕ , at each average latitude, $\langle \lambda \rangle$, by placing a straight edge across the space-time map so that it was parallel to the tracks, and then measuring the distance, Δt , intercepted between the ends of that straight edge at the top and bottom of the map. I calibrated this measurement in days, in terms of the 30-day length of the horizontal axis. During this time, the track spanned a vertical distance equal to $2R_\odot \cos(\lambda_2 - B_0)$ between the peaks of the serrated edges of the map, and the speed was given by

$$v_\phi(\langle \lambda \rangle) = \frac{2R_\odot \cos(\lambda_2 - B_0)}{\Delta t} = \frac{2R_\odot \cos(\langle \lambda \rangle - (\Delta\lambda/2) - B_0)}{\Delta t}, \quad (3)$$

where $\langle \lambda \rangle = (\lambda_1 + \lambda_2)/2$ and $\Delta\lambda = (\lambda_1 - \lambda_2)$. As usual, R_\odot is the solar radius, and $B_0 = 6.^\circ8$.

Figure 4 shows the resulting plot of speed versus latitude for the simulated faculae. Here, the red dashed line is a 2-parameter linear fit for the slope and polar speed. The rms scatter of 0.0089 km s^{-1} shows that the technique is able to estimate the speeds of the simulated faculae with a precision better than 0.01 km s^{-1} . With this precision, the polar offset is essentially 0, and the value of $v_0 = 1.97 \text{ km s}^{-1}$, which is only 0.03 km s^{-1} less than the value of 2.00 km s^{-1} that was assigned to the simulated faculae. The right panel shows the same data, but the dashed red line is a 1-parameter linear fit that is forced to pass through the point $(90, 0)$. In this case, the rms deviation from the line is 0.0090 km s^{-1} , which is only 0.0001 km s^{-1} larger than the value that was obtained in the two-parameter fit in the left panel. Also, $v_0 = 1.99 \text{ km s}^{-1}$, which is only 0.01 km s^{-1} less than the assigned value of 2.00 km s^{-1} . So this measuring technique does an excellent job of recovering the speed of the simulated faculae and gives confidence to the space-time approach.

3. SOLAR OBSERVATIONS

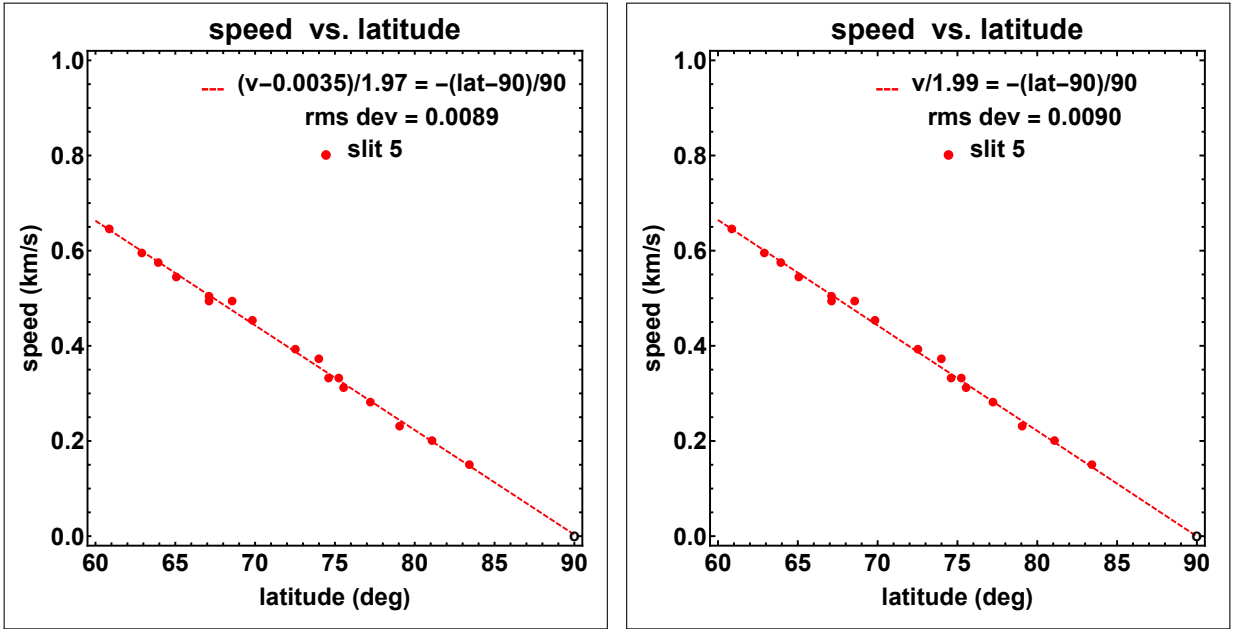


Figure 4. Speed-versus-latitude plots for simulated faculae. (left): The red dashed line is a 2-parameter linear fit for the slope and polar speed. (right): The red dashed line is a 1-parameter fit that is forced through the point (90, 0). The forced fit increases v_0 from 1.97 km s^{-1} to 1.99 km s^{-1} , reproducing the input profile of Eq(1) with an rms scatter less than 0.01 km s^{-1} .

3.1. MDI 6767 Å Faculae

With that understanding, I repeated the measurements of the Sun’s polar faculae, observed in the 6767 \AA continuum in 1997-1998 by the MDI instrument on SOHO. However, to track the observed faculae, I used a 3-pixel slit width, rather than the 5-pixel slit that I had used to measure the simulated faculae. Because the solar images were smaller than the simulated images ($R_{\odot} = 246$ pixels compared to 490 pixels), the slit widths were approximately the same size ($\sim 7 \text{ Mm}$ compared to $\sim 8.5 \text{ Mm}$). A small slit width might make it possible to obtain unique speeds at latitudes above 80° where the overlap of tracks from neighboring latitudes begins to be a limitation.

Figure 5 shows a sample of space-time maps obtained with a 3-pixel (8.5 Mm) slit at low, middle, and high polar latitudes, illustrating the different characteristics of the tracks of faculae at those latitudes. At middle latitudes ($72.^\circ 1$), the tracks are straight and parallel. At low latitudes ($69.^\circ 0$), the tracks are sparse and faint. At high latitudes ($82.^\circ 7$), the tracks are numerous with some variations of their slopes. Despite these differences, the average slope clearly decreases through this latitude range. This is a different selection of space-time maps than the ones shown in paper I. Thus, the reader can refer to paper I for additional examples of how the tracks vary with latitude in the $71\text{--}80^\circ$ range.

Figures 6 and 7 show plots of the measured speeds versus latitude. In these figures, the red points refer to measurements in the approximate $70\text{--}80^\circ$ range of latitudes where numerous parallel tracks were clearly visible. By comparison, the blue points refer to measurements outside that range where I had some difficulty in finding a unique speed, either because there were few parallel tracks (which happened at low latitude), or because the tracks were not all parallel (which happened at high latitude). In the left panel of Figure 6, the dashed black line is a 2-parameter, linear rms fit to all of the points, of the form

$$\frac{v - \Delta v}{v_0} = \frac{90 - \lambda}{90}, \quad (4)$$

where Δv is the projected speed at the Sun’s pole, v_0 is a speed proportional to the slope of the space-time track, and λ is the latitude in degrees. As one can see, this fit to all of the points gives $\Delta v = 0.027 \text{ km s}^{-1}$ and $v_0 = 1.85 \text{ km s}^{-1}$ with an rms scatter of 0.012 km s^{-1} . By comparison, in the right panel, the dashed red line is a similar fit that is limited to the 6 red points in the range $70\text{--}80^\circ$ where I had the greatest confidence in the measurements. As one can see, the linear fit to the red points gave $\Delta v = 0.026 \text{ km s}^{-1}$ and $v_0 = 1.87 \text{ km s}^{-1}$ with an rms scatter of 0.011 km s^{-1} . So this exclusion of the blue points did not change the result very much.

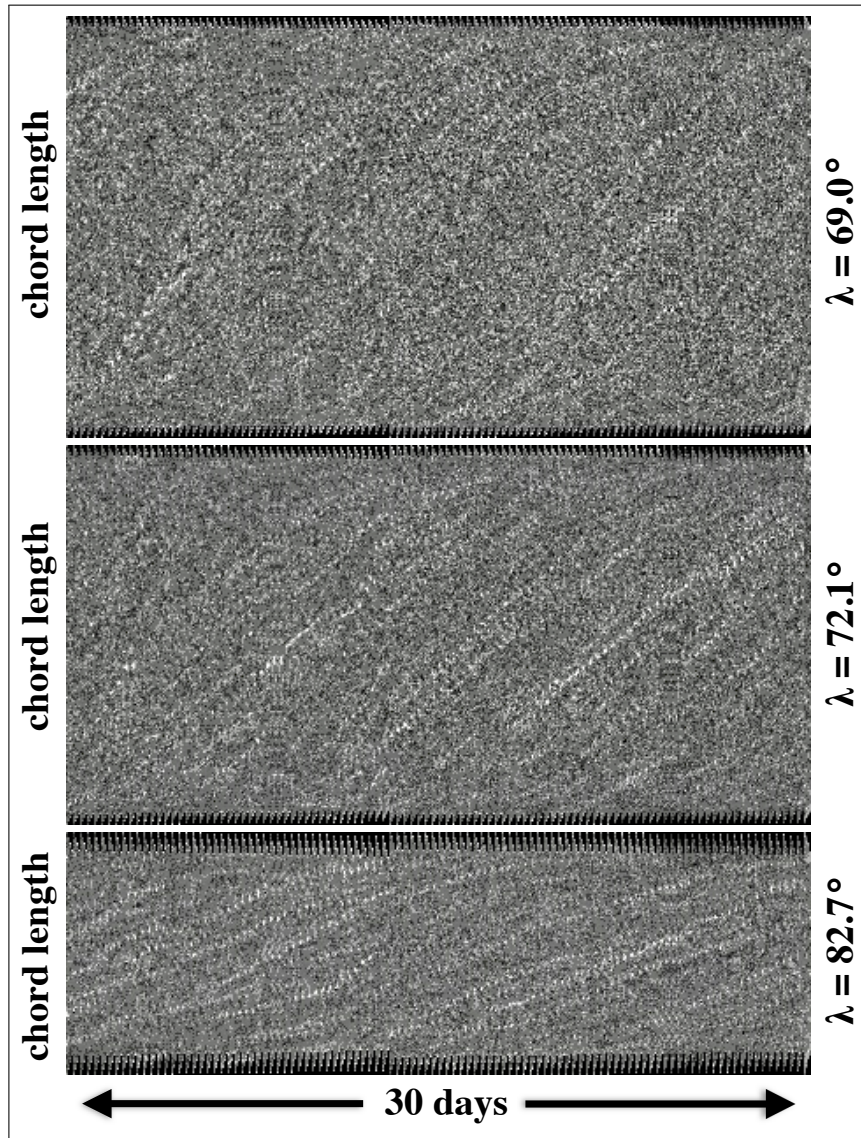


Figure 5. Space-time maps of 6767 Å continuum images obtained by the MDI instrument on SOHO during 7-21 February 1997-1998 using a 3-pixel slit. These maps show sparse and faint tracks at lower latitude, straight and parallel tracks at mid-latitude, and many tracks with slope variations at higher latitude. Yet, the trend from high speed to low speed is clearly visible.

Figure 7 shows similar plots, except that the dashed lines are 1-parameter fits that are forced to pass through the point (90, 0) where the speed at the pole is 0 km s⁻¹. In this case, $v_0 = 1.99$ km s⁻¹ for all of the points, and 2.01 km s⁻¹ when only the 6 red points were included. The rms deviations are 0.015 km s⁻¹ and 0.012 km s⁻¹, respectively.

3.2. HMI 6173 Å Magnetic Flux Elements

Historically, polar faculae have provided a way of inferring properties of the polar fields prior to the invention of the solar magnetograph (Babcock 1953; Sheeley 2008; Muñoz-Jaramillo et al. 2012). However, with improvements in the spatial resolution and sensitivity of magnetographs, the magnetic elements in the Sun’s polar caps at sunspot minimum may be as visible in maps of the Sun’s line-of-sight field as they are in flat-fielded images in the 6767 Å continuum (see Figure 5 of Sheeley & Warren (2006)). However, the ‘flat fielding’ is unnecessary in magnetograms, which are essentially differences of images with opposite circular polarization. So I thought that it would be relatively easy to extend the tracking measurements to observations of the magnetic field, especially when the polar fields were relatively strong and one of the poles was tipped favorably toward Earth.

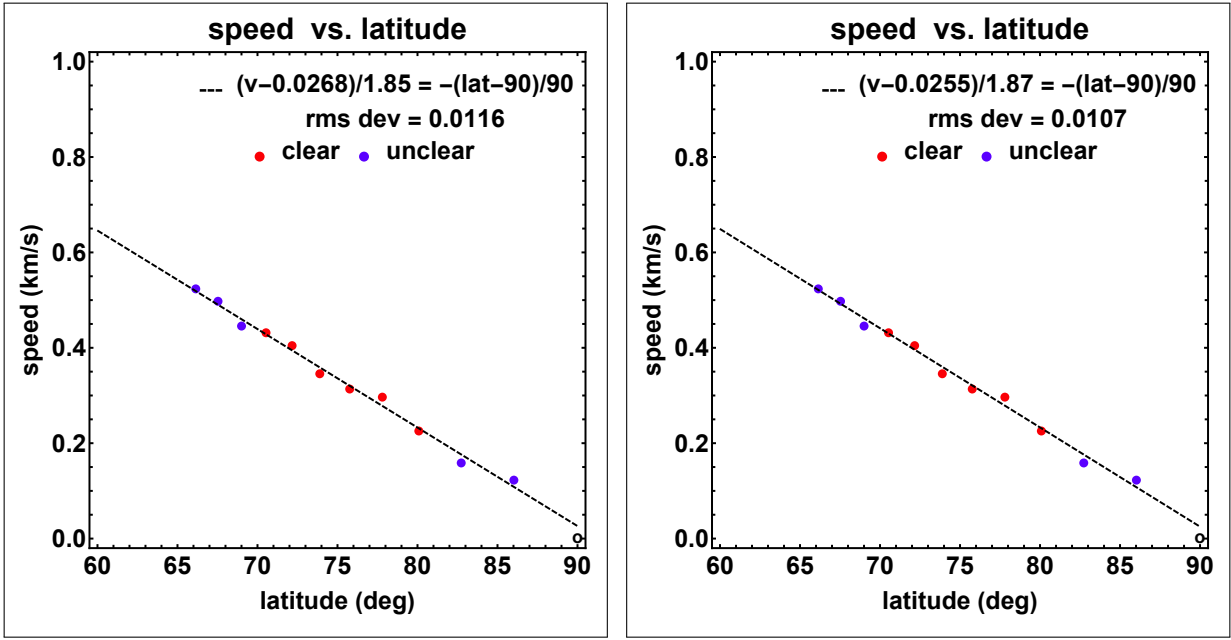


Figure 6. Speed versus latitude for faculae observed in the 6767 Å continuum with the MDI instrument on SOHO during February 1997-1998. The dashed black line (left panel) is the 2-parameter fit to all of the points, and the dashed red line (right panel) is the corresponding fit to only the more confidently observed red points (marked clear, compared to the blue points, marked unclear). The red points give a marginally better fit with a smaller polar-offset, a larger slope, and a smaller rms scatter.

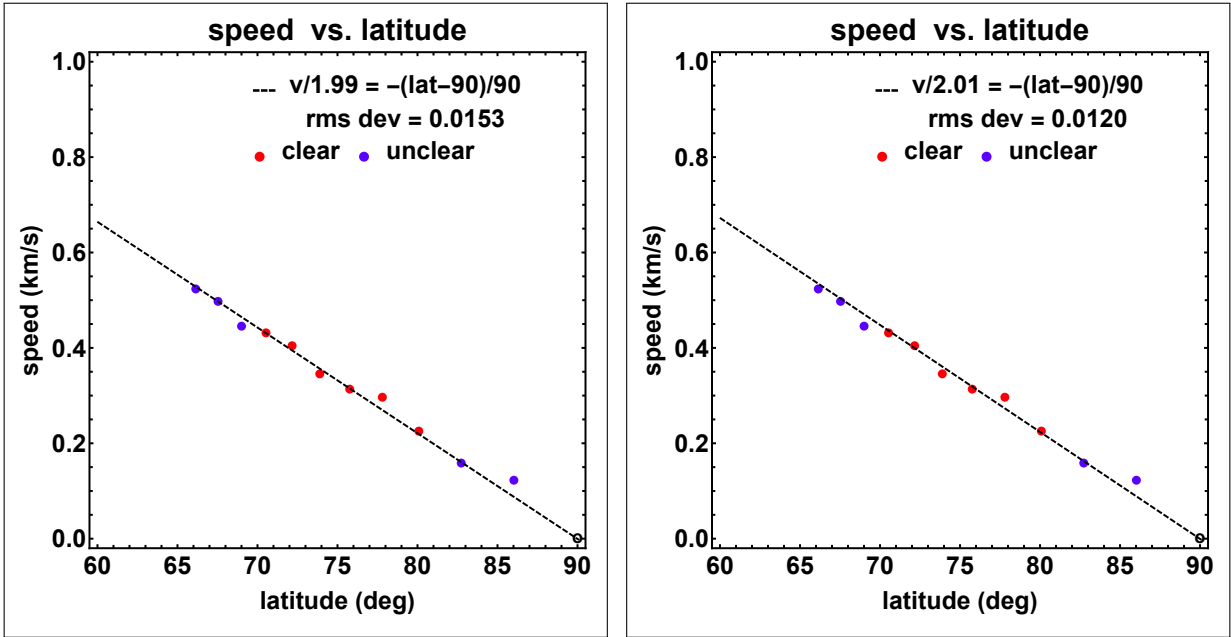


Figure 7. Same as Figure 6, except that the dashed lines are 1-parameter fits that were forced to go through the point (90, 0). These forced fits give larger slopes, about 2.0 km s^{-1} , and rms scatter that is only slightly larger than those in Figure 6.

Such magnetograms were obtained by the Helioseismic Magnetic Imager (HMI) on the *Solar Dynamics Observatory* (SDO) using the Zeeman-sensitive 6173 Å line. I downloaded jpeg versions of these images from the Joint Science Operations Center (JSOC) at Stanford University (<http://jsoc.stanford.edu/ajax/lookdata.html>), and processed them in the same way that I had processed the flat-fielded MDI images of the 6767 Å continuum. The HMI images consisted of 12-min averages obtained at 6-hr intervals during 1-15 September of 2017, 2018, and 2019. Each of these intervals is centered on September 7, when B_0 has its maximum value of $7.^\circ 25$ and Earth has its most favorable view of the

Sun's north polar region. Also, at this time, the perspective changes least with time, so that corrections for the B_0 variation during this 15-day interval are less than $\pm 0.^\circ 05$ (see Appendix A), and therefore negligible compared to other sources of error. Finally, during 2017-2019, the north polar field strength was near its maximum, according to observations at the Wilcox Solar Observatory (WSO) (<http://wso.stanford.edu>), which gave values approaching 1 Gauss. Consequently, the average number of magnetic flux elements and the corresponding number of polar faculae was near its maximum value for this particular sunspot cycle.

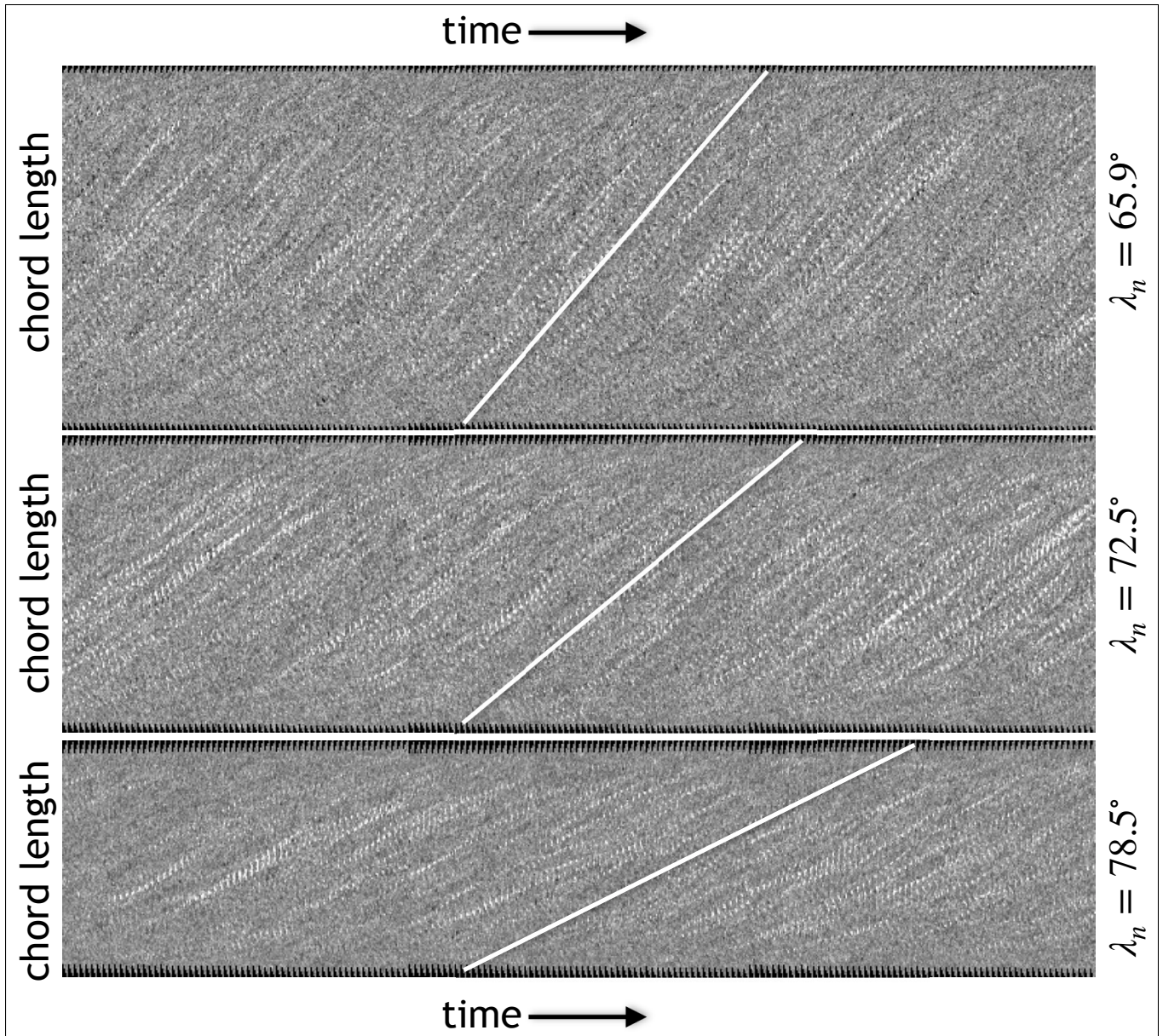


Figure 8. Space-time maps of HMI magnetograms during 1-15 September 2017, 2018, and 2019. These maps were obtained from 512 x 512 pixel jpeg images using a 3-pixel slit. White lines are superimposed to emphasize that the slopes tend to decrease with latitude. The horizontal axis spans 45 days, and the chord length is given approximately by $2R_{\odot} \cos(\lambda_n - 7.^\circ 25)$.

Figure 8 shows a sample of the resulting space-time maps of these HMI magnetograms obtained using a 3-pixel slit (corresponding to about 8.8 Mm for the 235-pixel radius of the solar image). Whereas the space-time maps of polar faculae in Figure 5 spanned 30 days during the two-year interval 7-21 February 1997-1998, these space-time maps of magnetic flux elements span 45 days during the three-year interval 1-15 September 2017-2019. I hoped the additional tracks from the third year would improve the statistics and make it easier to define the common slope of the

quasi-parallel tracks. White lines are superimposed on each panel to show the trend of the slopes (and thus speeds) to decrease with increasing latitude. Note that at the lowest latitude of 65.9° , the tracks of these magnetic elements are more visible than the tracks of polar faculae were at 69° in Figure 5.

Figure 9 supports this trend for the speeds to decrease with latitude. The data points deviate by 0.027 km s^{-1} from a best-fit straight line (left panel), and only 0.029 km s^{-1} from a straight line that is forced to reach 0 km s^{-1} at the pole (right panel). In this case, the equation of the line is given by Eq(1) with $v_0 = 2.11 \text{ km s}^{-1}$. As discussed in paper I, the speed, v_0 , corresponds to a synodic rotation rate of

$$\omega = \frac{v(\lambda)}{R_\odot \cos \lambda} = \frac{v_0(2/\pi)(\pi/2 - \lambda)}{R_\odot \sin(\pi/2 - \lambda)} \approx \frac{2}{\pi} \frac{v_0}{R_\odot}, \quad (5)$$

so that $v_0 = 2.11 \text{ km s}^{-1}$ gives a nearly constant synodic rotation rate of $\omega = 9.55 \text{ day}^{-1}$ at the north pole, and a synodic rotation period of 37.7 days.

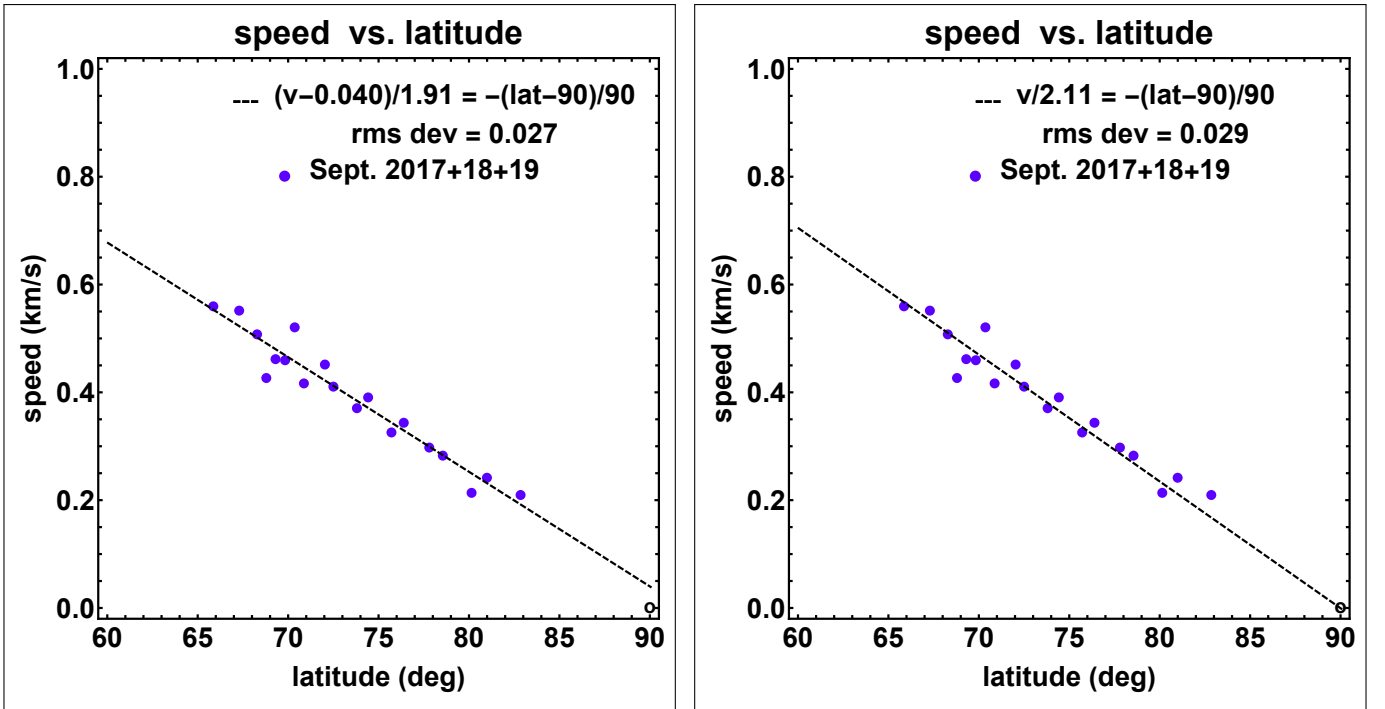


Figure 9. Speed versus latitude for flux elements observed with the HMI instrument on SDO during 1-15 September, 2017-2019. (left): the dashed line is a 2-parameter fit for slope and polar intercept; (right): a 1-parameter fit for the slope of the line that is forced to pass through the point $(90, 0)$. In this case, $v_0 = 2.11 \text{ km s}^{-1}$ and the rms scatter is 0.029 km s^{-1} .

3.3. Comparison With Previous Measurements Using Other Techniques

Figure 10 provides a graphic comparison between my measurements from space-time maps and previous measurements by other investigators. For this comparison, all of the measurements have been converted to sidereal rates expressed in $\mu\text{rad s}^{-1}$ and plotted versus latitude in the range $60\text{-}90^\circ$. These measurements come in pairs: First, the MWO magnetic measurements by Snodgrass (1983) (pink curve) and the HMI magnetic measurements by Liu & Zhao (2009) (solid blue curve) are nearly coincident at the top of the display. This near-perfect coincidence is surprising because the HMI observations have a much higher spatial resolution than the MWO observations. Second, the combined magnetic field measurements from the Huairou Solar Observatory (HSO) and the National Solar Observatory (NSO) by Deng et al. (1999) (dotdashed blue curve) lie only $\sim 0.02\text{-}0.04 \mu\text{rad s}^{-1}$ above the Doppler measurements of Howard & Harvey (1970) (red curve). Third, the polar faculae measurements by Müller (1954) (blue and green dots) and Waldmeier (1955) (pink dots) are scattered along a path surrounding the red curve of Howard & Harvey (1970). In particular, the best measurements by Müller (1954) (green dots) fall almost precisely along that red curve.

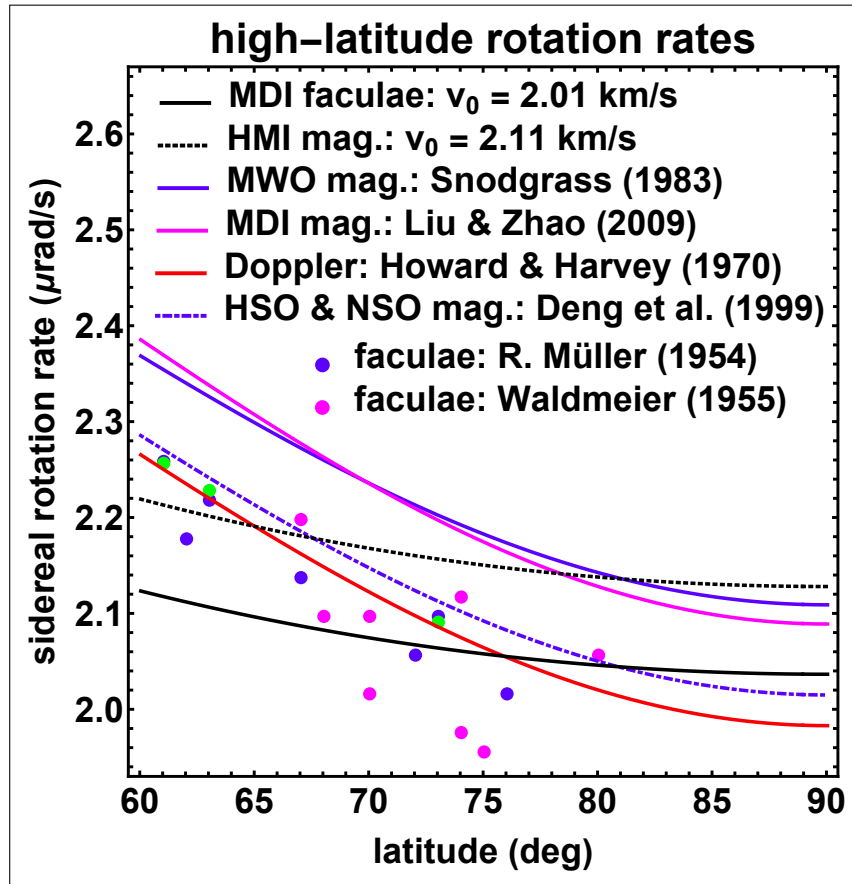


Figure 10. Sidereal rotation rates obtained from space-time maps of HMI magnetic flux (dashed, black curve) and MDI 6767 Å continuum faculae (solid, black curve), compared with prior measurements of magnetic flux by Snodgrass (1983) (blue curve), Liu & Zhao (2009) (pink curve), Deng et al. (1999) (dotdashed blue curve), MWO Doppler fields by Howard & Harvey (1970) (red curve), and polar faculae by Müller (1954) (blue and green dots) and Waldmeier (1955) (pink dots).

Moreover, the plots of all of these prior measurements have a common, parabolic-like shape, rising with increasing angular distance from a vertex at the Sun's pole.

These rising distributions are crossed by the two black curves of much lower slope representing my space-time measurements of HMI magnetic fields (dotted curve) and MDI observations of polar faculae (solid curve). Whereas the sidereal rotation rates of all of these measurements might be regarded as comparable, the relatively flat profiles of my space-time measurements differ noticeably from the quadratic profiles of the prior measurements. A characteristic of the prior measurements is that they were obtained by fitting the data points with a quartic sine-latitude profile of the form $\omega(\lambda) = A + B \sin^2 \lambda + C \sin^4 \lambda$, whose terms are not orthogonal and therefore might introduce crosstalk, according to Snodgrass (1983). Deng et al. (1999) appreciated this problem, but they were even more leery of using this profile because its latitude derivative vanishes at both the equator and the poles. They admitted that the derivative ought to vanish at the equator, where the rotation rate went through a maximum, but they knew of no physical reason why it ought to vanish at the poles. In fact, they mentioned that their measurements of the angular rotation rate were better matched by a linear approach to the poles. Nevertheless, despite these objections, they used the quartic formula to facilitate a comparison with the measurements of other observers.

In contrast, I measured the rotational speed, v , not the angular speed, ω , and only considered speeds in the range 65-85° latitude. In this case, the data points were well fit by a straight line that projected to 0 km s⁻¹ at the pole. If I had measured speeds all the way back to the equator, as some of the other investigators did, I might have obtained a curved distribution of points that required the quartic formula to achieve a good fit. In any case, the linear approach to 0 km s⁻¹ at the pole matched the linear decrease of the radius of the latitude contours, and gave a nearly constant angular rotation rate near the pole. This is the reason that my angular speed profiles were nearly flat - even flatter than the other curves, that were based on the quartic formula.

4. SUMMARY AND DISCUSSION

In paper I, I found a new way to measure the high-latitude rotation rate of the Sun by using space-time maps of polar faculae. Now, in this paper, I have tested this method using simulated polar faculae moving with a known speed profile. Space-time maps of the simulated faculae reproduced these motions with an accuracy better than 0.01 km s^{-1} , and also provided more information about space-time maps of polar faculae. Revised measurements of the original 6767 Å images gave a high-latitude angular rotation rate that is nearly constant over a polar cap of roughly 30° polar angle with a synodic rate of approximately $9.^\circ 1 \text{ day}^{-1}$ and a corresponding rotation period of 39.6 days. Next, I applied this same space-time approach to HMI magnetograms during 1-15 September 2017-2019 and again obtained a latitude-independent polar rotation rate, this time with a synodic angular speed of $9.^\circ 55 \text{ deg day}^{-1}$ and a synodic period of 37.7 days. By comparison, prior rotation measurements had a much steeper quartic dependence on $\sin \lambda$, but their extrapolated polar rotation rates had comparable values.

Deng et al. (1999) said that they knew of no physical reason why the latitude derivative of the angular rotation rate should vanish at the poles. However, I think one compelling reason is that my observed speeds, v_ϕ , showed a linear decrease to 0 km s^{-1} at the poles, which offset the corresponding linear decrease to 0 shown by the radius, $R_\odot \cos \lambda$, of the latitude contours. Consequently, the angular rotation rate, ω , is approximately constant over modest polar cap areas surrounding the poles. It reminded me of the polar and equatorial asymptotes that Sheeley & DeVore (1986) obtained in their analytical calculations of the decay of the Sun’s mean line-of-sight magnetic field. In that analysis, differential rotation wound the mid-latitude field into stripes of alternating polarity whose contributions cancelled out. Thus, the mean field was determined by the surviving unwound, non-axisymmetric flux at the poles and the equator. However, Sheeley & DeVore (1986) used the Newton & Nunn (1951) profile, $\omega(\lambda) = \omega_0 - \omega_1 \sin^2 \lambda$, whose latitude derivative also vanishes at the equator and the poles. So, these polar and equatorial flux concentrations resulted from the Newton & Nunn (1951) rotation profile, which is a special case of the quartic formula discussed above.

I explored two different ways of measuring the speeds. One determined the ‘peak-to-peak’ height of the space-time map from the measured latitude, λ_2 , of the longer edge of the slit indirectly, using the relation $\Delta x_2/R_\odot = 2 \cos(\lambda_2 - B_0)$. The other method determined Δx_2 directly by subtracting the measured pixel values of the x-coordinates at opposite ends of the longer edge of the slit, according to $\Delta x_2/R_\odot = (x_{2w} - x_{2e})/R_\odot$, where e and w refer to the east and west ends of the slit. Although these methods ought to have given the same result, the direct method gave values that were approximately 1% larger than the values obtained from the cosine formula. Also, this ratio increased slightly with latitude, especially at the highest latitudes where spatial resolution and finite pixel size become important. However, the angle, $\lambda_2 - B_0$, is a by-product of the measured quantity, y_2/R_\odot (via Eq(2)), so that this approach is really equivalent to obtaining the chord length from a measurement of y_2 using the formula $\Delta x_2/R_\odot = 2\sqrt{1 - (y_2/R_\odot)^2}$. Consequently, the very small differences between these two approaches result from the different treatment of measurement errors in the two expressions for the chord length. This is discussed further in Appendix C.

Although the results using the observed and simulated polar faculae validate the use of the space-time mapping technique, it is instructive to inquire what to expect theoretically. Consequently, in Appendix A, I have provided calculations of how the B_0 angle changes during the year, and in Appendix B, I describe what to expect for a straight slit as well as a slit that is curved along the latitude contours.

I have benefitted from comments from members of the heliophysics group during a presentation of some of this material at LPL/UA. Solar observations of polar faculae were obtained from an online version of a paper by Sheeley & Warren (2006). The idea for this work was triggered by an email exchange with Yi-Ming Wang (NRL). I am grateful to Phil Scherrer (Stanford) and Yang Liu (Stanford) for helping me to obtain HMI observations from the JSOC website. Also, I am grateful to the referee for reading the manuscript carefully and suggesting some helpful improvements.

APPENDIX

A. EFFECTIVE TILT ANGLE, B_0

The Sun’s rotational axis is tipped about $7.^\circ 25$ away from the normal to the ecliptic plane. About September 7 of each year, the Earth lies in this tipping plane and obtains its best view of the Sun’s north pole. However, as Earth moves westward in its orbit around the Sun, the effective tilt angle decreases and reaches 0 around December 7 when the Sun’s poles are equidistant from Earth. It is relatively easy to calculate this relation by taking the scalar product

of a unit vector pointing along the Sun's axis and a unit vector pointing outward along the Sun-Earth line. This scalar product is the cosine of the angle between those two axes, and is given by $\cos(\pi/2 - B_0)$, which is just $\sin B_0$.

If we represent the real 7.25° tilt angle by the symbol, γ , then in the observer's $x'y'z'$ coordinate system, the unit vector, \mathbf{e}_{Sun} , along the Sun's axis is

$$\mathbf{e}_{Sun} = \mathbf{e}_{x'} \sin \gamma + \mathbf{e}_{z'} \cos \gamma, \quad (\text{A1})$$

where $\mathbf{e}_{x'}$ is the unit vector outward along the Sun-Earth line, and $\mathbf{e}_{z'}$ is the unit normal to the ecliptic plane. (I am leaving unprimed axes for the Sun's coordinate system, as will be seen in the next subsection.) Then, if ψ represents the orbital angle through which Earth has moved, the new Sun-Earth unit vector, \mathbf{e}_{new} , will be

$$\mathbf{e}_{new} = \mathbf{e}_{x'} \cos \psi + \mathbf{e}_{y'} \sin \psi. \quad (\text{A2})$$

Thus, the scalar product of these two unit vectors is $\mathbf{e}_{Sun} \cdot \mathbf{e}_{new} = \sin \gamma \cos \psi$. Therefore,

$$\sin B_0 = \sin \gamma \cos \psi, \quad (\text{A3})$$

which reduces to

$$B_0 \approx \gamma \cos \psi \quad (\text{A4})$$

because γ and B_0 are small angles. Consequently, when $\psi = 0$, $B_0 = \gamma = 7.25^\circ$, and when $\psi = \pi/2$, $B_0 = 0^\circ$. So, if the Sun's south pole is tipped 7.25° toward Earth on March 7, then 21 days earlier on February 14, the effective tilt angle, B_0 , will be approximately $-7.25 \cos(2\pi \times 21/365) = -6.78^\circ$. This is close to the value of $B_0 = -6.8^\circ$ that is used in the text of this paper.

To interpret the tracks in our space-time maps, it is necessary to relate positions along the slit to spherical coordinates (R_\odot, θ, ϕ) relative to the Sun's poles. An important property of Eq(A3) and Eq(A4) is that they provide a way of transforming this relation from equations at the initial time when $\psi = 0$ and $B_0 = \gamma = 7.25^\circ$ to another time when $\psi \neq 0$ and $B_0 < \gamma$. To obtain the equations when the effective tilt is B_0 , we simply solve the problem when $\psi = 0$ and replace γ by B_0 .

B. THE SKY-PLANE SPEED AND SLIT POSITION

We begin with two Sun-centered coordinate systems. The first system is the observer's $x'y'z'$ coordinate system in which the x' axis points from the Sun to the observer, the z' axis is normal to the ecliptic plane, and the y' axis points to the right in a direction perpendicular to the $x'z'$ plane. The second system is the Sun's xyz coordinate system, in which the z axis points upward along the Sun's rotational axis. If the Sun's rotational axis were perpendicular to the ecliptic plane, then its three axes would coincide with the observer's $x'y'z'$ axes. However, the Sun's rotational axis is tipped 7.25° away from the normal to the ecliptic plane. As discussed in the previous subsection, we can assume that this is accomplished by a rotation of the Sun's coordinate system through an effective angle, B_0 , around the y axis. As indicated in Eqs(A3) and (A4), B_0 slowly oscillates from $+7.25^\circ$ to -7.25° and back in a year, as Earth (and the SOHO spacecraft) undergo their orbital motion around the Sun. Thus, at a given time, the two coordinate systems are related by the rotational transformation

$$\begin{pmatrix} x'/R_\odot \\ y'/R_\odot \\ z'/R_\odot \end{pmatrix} = \begin{pmatrix} \cos B_0 & 0 & \sin B_0 \\ 0 & 1 & 0 \\ -\sin B_0 & 0 & \cos B_0 \end{pmatrix} \begin{pmatrix} x/R_\odot \\ y/R_\odot \\ z/R_\odot \end{pmatrix} = \begin{pmatrix} \cos B_0 & 0 & \sin B_0 \\ 0 & 1 & 0 \\ -\sin B_0 & 0 & \cos B_0 \end{pmatrix} \begin{pmatrix} \sin \theta \cos \phi \\ \sin \theta \sin \phi \\ \cos \theta \end{pmatrix} \quad (\text{B5})$$

Consequently, in the Earth's coordinate system, the $x'y'z'$ coordinates are related to the Sun's spherical polar coordinates (R_\odot, θ, ϕ) by the equations:

$$x'/R_\odot = \sin \theta \cos \phi \cos B_0 + \cos \theta \sin B_0 \quad (\text{B6a})$$

$$y'/R_\odot = \sin \theta \sin \phi \quad (\text{B6b})$$

$$z'/R_\odot = -\sin \theta \cos \phi \sin B_0 + \cos \theta \cos B_0, \quad (\text{B6c})$$

where R_\odot is the solar radius. The same rotation applies to the longitudinal speed, $v_\phi = v_1$, tangent to the circular contours of constant latitude. In the Sun's xyz coordinate system, this speed is

$$\mathbf{v} = v_1(\cos \phi \mathbf{e}_y - \sin \phi \mathbf{e}_x), \quad (\text{B7})$$

and in the transformed $x'y'z'$ system, the coordinates are

$$\begin{pmatrix} v_{x'}/v_1 \\ v_{y'}/v_1 \\ v_{z'}/v_1 \end{pmatrix} = \begin{pmatrix} \cos B_0 & 0 & \sin B_0 \\ 0 & 1 & 0 \\ -\sin B_0 & 0 & \cos B_0 \end{pmatrix} \begin{pmatrix} -\sin \phi \\ \cos \phi \\ 0 \end{pmatrix} = \begin{pmatrix} -\sin \phi \cos B_0 \\ \cos \phi \\ \sin \phi \sin B_0 \end{pmatrix} \quad (\text{B8})$$

Now, I am going to select the $y'z'$ sky-plane components of position and speed from Eqs(B6) and (B8), and relabel them in terms of a new xy coordinate system in which $y' \rightarrow x$ and $z' \rightarrow y$. Also, I am going to replace the polar angle, θ , by north latitude, λ , defined by $\lambda = \pi/2 - \theta$. The result is

$$x/R_\odot = \cos \lambda \sin \phi \quad (\text{B9a})$$

$$y/R_\odot = -\cos \lambda \cos \phi \sin B_0 + \sin \lambda \cos B_0 \quad (\text{B9b})$$

$$v_x/v_1 = \cos \phi \quad (\text{B9c})$$

$$v_y/v_1 = \sin \phi \sin B_0. \quad (\text{B9d})$$

Our objective is to solve these equations for two cases. In case 1, the slit is curved and follows a contour of constant latitude, λ_0 . The analysis of this case will help us to decide whether it would be useful to make space-time maps with a curved slit sometime in the future. In case 2, the slit is a straight chord whose vertical position has the constant value $y/R_\odot = \sin(\lambda_0 - B_0)$. The analysis of this case will help us to interpret the space-time maps and their measurements in paper I and in the text of this paper.

B.0.1. *The curved slit*

The curved slit is obtained by setting $\lambda = \lambda_0$ in Eqs(B9a) through (B9d). Taking the time derivative of Eq(B9a) and replacing dx/dt by $v_1 \cos \phi$ as given by Eq(B9c), we obtain

$$\frac{1}{R_\odot} \frac{dx}{dt} = \cos \lambda_0 \cos \phi \frac{d\phi}{dt} = \frac{v_1}{R_\odot} \cos \phi. \quad (\text{B10})$$

Assuming that $\cos \phi \neq 0$, it follows that $d\phi/dt = v_1/R_\odot \cos \lambda_0$, which integrates to give

$$\phi = \frac{v_1 t}{R_\odot \cos \lambda_0}. \quad (\text{B11})$$

Consequently, the time dependence of x , y , v_x , and v_y are obtained by substituting this value of ϕ into Eqs(B9a)-(B9d) with λ replaced by λ_0 :

$$x/R_\odot = \cos \lambda_0 \sin \left(\frac{v_1 t}{R_\odot \cos \lambda_0} \right) \quad (\text{B12a})$$

$$y/R_\odot = -\cos \lambda_0 \cos \left(\frac{v_1 t}{R_\odot \cos \lambda_0} \right) \sin B_0 + \sin \lambda_0 \cos B_0 \quad (\text{B12b})$$

$$v_x/v_1 = \cos \left(\frac{v_1 t}{R_\odot \cos \lambda_0} \right) \quad (\text{B12c})$$

$$v_y/v_1 = \sin \left(\frac{v_1 t}{R_\odot \cos \lambda_0} \right) \sin B_0. \quad (\text{B12d})$$

This is the curved-slit solution to Eqs(B9a)-(B9d).

The latitude contours are obtained by eliminating the time dependence between Eqs(B12a) and (B12b):

$$\left(\frac{x/R_\odot}{\cos \lambda_0} \right)^2 + \left(\frac{y/R_\odot - \sin \lambda_0 \cos B_0}{\cos \lambda_0 \sin B_0} \right)^2 = 1. \quad (\text{B13})$$

Eq(B13) describes an ellipse whose center lies at $(x, y) = (0, R_\odot \sin \lambda_0 \cos B_0)$, with a semi-major axis $a = R_\odot \cos \lambda_0$ and a semi-minor axis $b = R_\odot \cos \lambda_0 \sin B_0 \ll a$. These are the contours that are typically plotted on Stonyhurst grids and in Figure 1 of this paper. (See, for example, <https://solar-center.stanford.edu/solar-images/latlong.html>).

Finally, despite the relatively simple solution given by Eqs(B11) and (B12a-d), a space-time plot follows the motion along the curved elliptical path, not along the x -axis. For this purpose, it is necessary to evaluate the speed along this curved path, which is easily found by combining Eqs(B12c) and (B12d):

$$v/v_1 = \sqrt{(v_x/v_1)^2 + (v_y/v_1)^2} = \sqrt{1 - \sin^2 \phi \cos^2 B_0}, \quad (\text{B14})$$

with ϕ given by Eq(B11). Now, because this speed, v , and the curved path length, s , are related by $ds/dt = v$, it follows that the path length is given by the elliptic integral

$$s/R_\odot = \cos \lambda_0 \int_0^\phi \sqrt{1 - \sin^2 \phi \cos^2 B_0} d\phi, \quad (\text{B15})$$

where $\phi = t/(\tau \cos \lambda_0)$ and $\tau = R_\odot/v_1$. Here, the upper limit of integration, ϕ , must be less than ϕ_{max} , the longitude where the ellipse given by Eq(B13) intersects a circle corresponding to the Sun's limb. Those coordinates are:

$$x_{limb}/R_\odot = \sqrt{1 - \left(\frac{\sin \lambda_0}{\cos B_0}\right)^2} \quad (\text{B16a})$$

$$y_{limb}/R_\odot = \frac{\sin \lambda_0}{\cos B_0} \quad (\text{B16b})$$

$$\sin \phi_{max} = \frac{x_{limb}/R_\odot}{\cos \lambda_0} = \left(\frac{1}{\cos \lambda_0}\right) \sqrt{1 - \left(\frac{\sin \lambda_0}{\cos B_0}\right)^2} \quad (\text{B16c})$$

From Eqs(B16c) and (B14), it follows that the speed, v_{limb} , at each end of the curved slit is given by

$$\frac{v_{limb}}{v_1} = \frac{\sin B_0}{\cos \lambda_0}. \quad (\text{B17})$$

Note that for small B_0 the integral in Eq(B15) reduces to $\sin \phi$, and s/R_\odot reduces to x/R_\odot given by Eq(B12a). This means that for a small effective tilt angle, B_0 , the curved-slit solution reduces to the straight-slit solution.

B.0.2. The straight slit

The straight-slit equations correspond to y/R_\odot equal to a constant obtained by setting $x/R_\odot = 0$ in Equation (B13) and taking the favorable-view solution (for the northern hemisphere when $B_0 > 0$):

$$y/R_\odot = \sin(\lambda_0 - B_0). \quad (\text{B18})$$

In this case, the slit crosses several latitude contours, and toward the end of the slit, the speed, v_x becomes negative and the speed, v_y , reaches a maximum and then decreases. To understand this, we return to Eqs(B9a-d) with y/R_\odot replaced by $\sin(\lambda_0 - B_0)$, as given in Eq(B18). The idea is to express each parameter in terms of the latitude, λ , and then to relate them parametrically. First, Eq(B9b) gives

$$\cos \phi(\lambda) = \frac{\sin \lambda \cos B_0 - \sin(\lambda_0 - B_0)}{\cos \lambda \sin B_0}. \quad (\text{B19})$$

Consequently, x/R_\odot , v_x/v_1 , and v_y/v_1 can all be expressed in terms of λ using $\cos \phi(\lambda)$ given by Eq(B19):

$$x/R_\odot = \cos \lambda \sqrt{1 - \cos^2 \phi(\lambda)} \quad (\text{B20a})$$

$$v_x/v_1 = \cos \phi(\lambda) \quad (\text{B20b})$$

$$v_y/v_1 = \sin B_0 \sqrt{1 - \cos^2 \phi(\lambda)}. \quad (\text{B20c})$$

Next, we introduce the time, t , using Eq(B20b) written as

$$\frac{1}{v_1} \frac{dx(\lambda)}{dt} = \cos \phi(\lambda). \quad (\text{B21})$$

In this case,

$$v_1 t = \int_{\lambda_0}^\lambda \frac{dx(\lambda)}{\cos \phi(\lambda)} = \int_{\lambda_0}^\lambda \frac{1}{\cos \phi(\lambda)} \frac{dx(\lambda)}{d\lambda} d\lambda. \quad (\text{B22})$$

Recall that λ has its maximum value, λ_0 , at the center of the slit where $x = 0$, and that λ decreases as x increases. Consequently, in Eq(B22), the factor, $dx(\lambda)/d\lambda$ is negative and the upper limit of integration, λ , must be less than λ_0 . Also, to keep the denominator of the integrand from vanishing, λ must be greater than the value, λ_1 , where $v_x = 0$ and $\phi(\lambda_1) = \pi/2$. From Eqs(B20b) and (B19), this latitude, λ_1 , is given by

$$\sin \lambda_1 = \sin(\lambda_0 - B_0) / \cos B_0. \quad (\text{B23})$$

Substituting the value of $x(\lambda)$ from Eq(B20a) into Eq(B22), we get

$$\frac{t}{\tau} = \int_{\lambda_0}^{\lambda} \frac{1}{\cos \phi(\lambda)} \frac{d}{d\lambda} \left\{ \cos \lambda \sqrt{1 - \cos^2 \phi(\lambda)} \right\} d\lambda, \quad (\text{B24})$$

where $\tau = R_{\odot}/v_1$, $\lambda_0 > \lambda > \lambda_1$, and $\cos \phi(\lambda)$ is given by Eq(B19).

Although the time, t , suffers a discontinuity where $\lambda = \lambda_1$, other parameters like x , v_x , and v_y extend continuously across $\lambda = \lambda_1$ to an even smaller value of $\lambda = \lambda_2$ at the ends of the slit. This second latitude is obtained by setting the maximum value of x/R_{\odot} , which is $\cos(\lambda_0 - B_0)$, equal to $\cos \lambda \sqrt{1 - \cos^2 \phi(\lambda)}$, as given by Eq(B20a), and solving for λ . The result is

$$\sin \lambda_2 = \sin(\lambda_0 - B_0) \cos B_0. \quad (\text{B25})$$

So the center of the straight slit is tangent to the latitude contour where $\lambda = \lambda_0$ and the sky-plane speed is v_1 . Progressing along the slit, the latitude remains approximately constant for a while, but then decreases as the contours bend poleward, and are replaced by lower-latitude contours toward the limbs. The speed, v_x , also decreases, reaching 0 when $\lambda = \lambda_1$, and becoming increasingly more negative as the latitude continues to decrease. Physically, the reason for this negative speed is that $\phi(\lambda)$ has reached $\pi/2$, and for larger values of ϕ , the tangential component of speed, $v_1 \mathbf{e}_{\phi}$, is pointing backward along the slit. Eventually, $\lambda = \lambda_2$ at the end of the slit, where the speed is

$$\frac{v_x}{v_1} = - \frac{\tan(\lambda_0 - B_0) \sin B_0}{\sqrt{1 + \tan^2(\lambda_0 - B_0) \sin^2 B_0}} = - \sin \xi_0, \quad (\text{B26})$$

where the angle, ξ_0 , is defined by $\tan \xi_0 = \tan(\lambda_0 - B_0) \sin B_0$.

Eqs(B20a) and (B23) give the slit position for which the speed, $v_x = 0$. However, that slit position is expressed in terms of the solar radius, R_{\odot} . What we really want is the slit position relative to the half length of the slit at that latitude. This ratio is given by

$$\frac{x_1}{x_{end}} = \frac{\cos \lambda_1}{\cos(\lambda_0 - B_0)} = \left(\frac{1}{\cos B_0} \right) \sqrt{1 - \left\{ \frac{\sin B_0}{\cos(\lambda_0 - B_0)} \right\}^2} \quad (\text{B27})$$

Thus, in Figure 3 with $\lambda_0 = 68.^{\circ}52$ and $B_0 = 6.^{\circ}8$, $x_1/x_{end} = 0.975$, which is very close to the edge of the space-time map. Likewise, in Figure 2 with $\lambda_0 = 77.^{\circ}18$ and $B_0 = 6.^{\circ}8$, $x_1/x_{end} = 0.942$, which is slightly farther from the limbs, as noted in Figures 2 and 3 of the text. Likewise, the short tracks of negative speed in the serrated edges of the space-time maps in Figures 2 and 3 must be tracks of faculae motions beyond the boundary where $v_x = 0$.

Eq(B27) indicates how x_1/x_{end} varies with latitude, λ_0 . We can see this by expanding the radical for small values of $\sin B_0$ and setting $\cos B_0 = 1$:

$$\frac{x_1}{x_{end}} \approx 1 - \frac{1}{2} \left(\frac{\sin B_0}{\cos(\lambda_0 - B_0)} \right)^2 \quad (\text{B28})$$

We can see that if λ_0 increases, x_1/x_{end} will decrease. Thus, when the slit is placed at a relatively high latitude in the polar cap, the sinusoidal tracks will be shorter, leaving more room for the other short tracks at the ends of the slit.

In summary, when $B_0 \neq 0$, space-time maps with curved or straight slits each have special complexities toward the limb. The best solution is to avoid the limbs and confine one's measurements to linear tracks at the central meridian.

C. TWO METHODS OF EVALUATING THE CHORD LENGTH, ΔX_2 , OF THE SLIT

As discussed in the text, at each latitude, the Sun's rotational speed in km s^{-1} was determined by measuring the average slope of the tracks in a space-time map. I determined this slope at the center of the chord by measuring the

time that a linear fit took to cross the vertical distance between the peaks of the serrated edges at the top and bottom of the map. The time in days was calibrated in terms of the horizontal length of the map, which was 30 days for the two-year interval that I used for polar faculae in 1997-1998 and 45 days for the three-year interval that I used for magnetic flux elements in 2017-2019. Once this had been done, it was necessary to measure the chord length, Δx_2 , of the longest edge of the slit, which was responsible for the peaks in the serrated edges of the space-time map.

There were two ways of evaluating Δx_2 . One way was to use the measured locations of the ends of the slit at the Sun's east and west limbs, and to subtract their column numbers, x_{2e} and x_{2w} , to obtain $\Delta x_2 = x_{2w} - x_{2e}$, in pixels. The other way was to calculate $2 \cos(\lambda_2 - B_0)$ using the value of λ_2 that I had already calculated from $y_2/R_\odot = \sin(\lambda_2 - B_0)$. However, because $2 \cos(\lambda_2 - B_0) = 2\sqrt{1 - (y_2/R_\odot)^2}$, this meant that $\lambda_2 - B_0$ was just an intermediary, and that I was really deriving Δx_2 from y_2 , the measured coordinate at the edge of the slit.

To understand the difference between these two approaches, we must recognize that the solar image is composed of many small, square pixels. For a particular row of pixels with $y = y_2$, we can calculate the corresponding x -value at the limb using $x = \sqrt{R_\odot^2 - y_2^2}$. However, even though y_2 and R_\odot are both integers, the derived quantity, $\sqrt{R_\odot^2 - y_2^2}$, is not an integer (except at the 'equatorial' and 'polar' limbs where R_\odot is defined). So in one case, we use $\Delta x_2 = x_{2w} - x_{2e}$ and call it $2x_2$, while in the other case, we use $2x = 2\sqrt{R_\odot^2 - y_2^2}$. We are interested in the difference, $\Delta x_2 - 2x$, and the ratio, $\Delta x_2/2x$, of these two quantities.

Let's consider a few examples. First, when $\lambda_2 = 66.^\circ 5$, I measured (row, column) values of (55, 136) and (55, 377) at the two ends of the chord. In this case, $\Delta x_2 = 241$ and $y_2 = 257 - 55 = 202$. Consequently, $x = \sqrt{(235)^2 - (202)^2} = 120.0875$, and $2x = 240.1749$. Therefore, $\Delta x_2 - 2x = 0.8251$. So the difference between the observed and derived length of the chord is about 0.8 pixel. Also, the ratio, $\Delta x_2/2x = 241/240.1749 = 1.0034$, which means that the direct determination of the length of the chord using $\Delta x_2 = x_{2w} - x_{2e}$ gives a value that is about 0.3% larger than the value derived from the measured value of y_2 . Note that $0.8251/241 = 0.0034$, suggesting that the correction, $\Delta x_2/2x - 1$, is given by the difference, $\Delta x_2 - 2x$, divided by the length of the chord, Δx_2 . (This conjecture is readily proved by defining the error, $\epsilon = (\Delta x_2/2x) - 1$ and the pixel difference divided by the chord length as $\delta = (\Delta x_2 - 2x)/\Delta x_2$. After some algebra, it follows that $\epsilon = \delta/(1 - \delta) \approx \delta + \delta^2 \approx \delta$.)

Second, when $\lambda_2 = 77.^\circ 4$, the measured coordinates were (36, 175) and (36, 338), giving a shorter chord with $\Delta x_2 = 163$ and $y_2 = 257 - 36 = 221$. Consequently, $x = \sqrt{(235)^2 - (221)^2} = 79.8999$, and $2x = 159.7999$. So, in this case, the difference is larger with $\Delta x_2 - 2x = 3.2001$ pixels. The ratio, $\Delta x_2/2x = 163/159.7999 = 1.0200$, so the direct determination is 2% larger than the indirect determination of the chord length. And the pixel ratio is $3.2001/163 = 0.0196$, very close to the error estimate of 0.0200.

Although there is a trend for this pixel-related correction to increase with latitude, especially toward the high-latitude end of the range, the increase is intermittent, and often a neighboring latitude will have a much smaller correction. To see this, consider, a third case, in which $\lambda_2 = 75.^\circ 3$. Here, the (row, column) coordinates were (39, 168) and (39, 345), corresponding to a chord length, $\Delta x_2 = 177$ and $y_2 = 257 - 39 = 218$. Now, $x = \sqrt{(235)^2 - (218)^2} = 87.7553$, and $2x = 175.5107$. Now, the difference and the ratio are both smaller with $\Delta x_2 - 2x = 1.4893$ pixels and $\Delta x_2/2x = 177/175.5107 = 1.0085$. The latitude is only $2.^\circ 1$ less than in the prior example, but the correction is much smaller.

REFERENCES

- Babcock, H. W. 1953, ApJ, 118, 387, doi: [10.1086/145767](https://doi.org/10.1086/145767)
- Deng, Y., Wang, J., & Harvey, J. 1999, SoPh, 186, 13, doi: [10.1023/A:1005186016971](https://doi.org/10.1023/A:1005186016971)
- Howard, R., & Harvey, J. 1970, SoPh, 12, 23, doi: [10.1007/BF02276562](https://doi.org/10.1007/BF02276562)
- Liu, Y., & Zhao, J. 2009, SoPh, 260, 289, doi: [10.1007/s11207-009-9450-6](https://doi.org/10.1007/s11207-009-9450-6)
- Muñoz-Jaramillo, A., Sheeley, N. R., Zhang, J., & DeLuca, E. E. 2012, ApJ, 753, 146, doi: [10.1088/0004-637X/753/2/146](https://doi.org/10.1088/0004-637X/753/2/146)
- Müller, R. 1954, ZA, 35, 61
- Newton, H. W., & Nunn, M. L. 1951, MNRAS, 111, 413, doi: [10.1093/mnras/111.4.413](https://doi.org/10.1093/mnras/111.4.413)
- Sheeley, N. R., J. 2008, ApJ, 680, 1553, doi: [10.1086/588251](https://doi.org/10.1086/588251)
- Sheeley, N. R., J., & DeVore, C. R. 1986, SoPh, 103, 203, doi: [10.1007/BF00147824](https://doi.org/10.1007/BF00147824)
- Sheeley, N. R., J., & Warren, H. P. 2006, ApJ, 641, 611, doi: [10.1086/500392](https://doi.org/10.1086/500392)
- Sheeley, N. R. 2024, ApJ, 976, 73, doi: [10.3847/1538-4357/ad85d0](https://doi.org/10.3847/1538-4357/ad85d0)
- Snodgrass, H. B. 1983, ApJ, 270, 288, doi: [10.1086/161121](https://doi.org/10.1086/161121)
- Waldmeier, M. 1955, ZA, 38, 37